

1  
2  
3  
4  
5  
6  
7  
8  
9  
10  
11  
12  
13  
14  
15  
16  
17  
18  
19  
20  
21  
22  
23  
24  
25  
26  
27  
28  
29  
30  
31  
32  
33  
34  
35  
36  
37  
38  
39  
40  
41  
42  
43  
44  
45  
46

**Realistic 3D computer model of the gerbil middle ear,  
featuring accurate morphology  
of bone and soft tissue structures**

**Jan A.N. Buytaert<sup>1,°</sup>, W.H.M. Salih<sup>1</sup>, M. Dierick<sup>2</sup>,  
P. Jacobs<sup>2</sup> and Joris J.J. Dirckx<sup>1</sup>**

<sup>1</sup> Laboratory of BioMedical Physics – University of Antwerp,  
Groenenborgerlaan 171, B-2020 Antwerp, Belgium  
<sup>2</sup> Centre for X-ray Tomography - Ghent University  
Proeftuinstraat 86, B-9000 Gent, Belgium

Running title: Accurate 3D gerbil ME model

<sup>°</sup> Corresponding author:  
email [jan.buytaert@ua.ac.be](mailto:jan.buytaert@ua.ac.be);  
telephone 0032 3 265 3553;  
fax 0032 3 265 3318.

## 47 ABSTRACT

48

49 In order to improve realism in middle ear (ME) finite element modeling (FEM),  
50 comprehensive and precise morphological data are needed. To date, micro-scale X-ray  
51 computed tomography ( $\mu$ CT) recordings have been used as geometric input data for FEM  
52 models of the ME ossicles. Previously, attempts were made to obtain this data on ME soft  
53 tissue structures as well. However, due to low X-ray absorption of soft tissue, quality of  
54 these images is limited. Another popular approach is using histological sections as data for  
55 3D models, delivering high in-plane resolution for the sections, but the technique is  
56 destructive in nature and registration of the sections is difficult.

57 We combine data from high-resolution  $\mu$ CT recordings with data from high-resolution  
58 orthogonal-plane fluorescence optical-sectioning microscopy (OPFOS), both obtained on the  
59 same gerbil specimen. State-of-the-art  $\mu$ CT delivers high-resolution data on the three-  
60 dimensional shape of ossicles and other ME bony structures, while the OPFOS setup  
61 generates data of unprecedented quality both on bone and soft tissue ME structures.

62 Each of these techniques is tomographic and non-destructive, and delivers sets of  
63 automatically aligned virtual sections. The datasets coming from different techniques need  
64 to be registered with respect to each other. By combining both datasets, we obtain a  
65 complete high-resolution morphological model of all functional components in the gerbil  
66 ME. The resulting three-dimensional model can be readily imported in FEM software and is  
67 made freely available to the research community.

68 In this paper, we discuss the methods used, present the resulting merged model and discuss  
69 morphological properties of the soft tissue structures, such as muscles and ligaments.

70

71

72

## 73 KEYWORDS:

74 gerbil, middle ear, modeling, high-resolution, three-dimensional, soft tissue, surface mesh,  
75 micro-scale X-ray computed tomography (micro-CT), orthogonal-plane fluorescence optical-  
76 sectioning microscopy (OPFOS)

77

78

79

## 80 INTRODUCTION

81

82 The middle ear (ME) forms a small three-dimensional (3D) biomechanical system. It mainly  
83 consists of the tympanic membrane (TM), three ossicles – malleus, incus and stapes – and  
84 their supporting ligaments and muscles. The remarkable performance of ME mechanics is  
85 too complex to be understood intuitively. For better understanding, ME modeling was  
86 introduced. Finite-element (computer) modeling (FEM) has become an established  
87 numerical technique to simulate ME mechanics. In ME research, the technique was first  
88 introduced by Funnell and Laszlo, 1978. As one of its inputs, FEM requires 3D morphological  
89 computer models of the ME components. These mesh models consist of a finite number of  
90 elements, e.g. tetrahedra or hexahedra.

91

92 Current morphological models are either incomplete, low resolution and/or contain  
93 rudimentary shapes to represent (some) ME components. Pioneering work in this field used  
94 manually drawn geometrical shapes in the computer to represent the ME malleus, incus and  
95 stapes (Wada et al., 1992; Ladak and Funnell, 1996; Blayney et al., 1997; Eiber et al., 2000;  
96 Prendergast et al., 2000; Koike et al., 2002). Some authors used low or modest resolution  
97 shapes measured with medical X-ray computed tomography (CT) (Rodt et al., 2002; Lee et  
98 al., 2006) or with tabletop micro-CT ( $\mu$ CT) devices (Decraemer et al., 2002; 2003; Elkhouri et  
99 al., 2006; Puria and Steele, 2010; Lee et al., 2010). Other authors used histological sectioning  
100 (Funnell et al., 1992; Sun et al., 2002) or magnetic resonance microscopy (MRM, NMR, MRI)  
101 (Funnell et al., 2005; Elkhouri et al., 2006), but again with modest resolutions. In many  
102 models, the suspensory ligaments and muscle tendons are either omitted (Wada et al. 1992;  
103 Ladak & Funnell 1996; Blayney et al. 1997; Lord et al. 1999; Rodt et al. 2002) or manually  
104 incorporated as simple geometrical objects such as blocks, cylinders or cones (Prendergast  
105 et al. 2000; Beer et al. 2000; Koike et al. 2002; Sun et al. 2002; Lee et al. 2006). To the  
106 authors' knowledge, only models by Wang et al., 2006; Gan et al., 2007; Cheng and Gan,  
107 2008 (using histological sectioning) and by Mikhael et al., 2004; Sim and Puria, 2008; Ruf et  
108 al., 2009 (using X-ray techniques) contain actually measured shapes of soft tissue structures,  
109 but in low resolution.

110

111 To improve realism in FEM calculations, ME geometry models need to incorporate all and  
112 accurate shapes of the ossicles and suspensory soft tissue structures (Decraemer et al.,  
113 2003). As the computer calculating capacity has grown to a point where it can manage large  
114 amounts of data, and as the scientific measurement apparatus is now capable of high-  
115 resolution imaging on all kinds of tissue types, the time has come to incorporate realistic and  
116 complete morphological 3D ME models in FEM. We point out that it might not be necessary,  
117 even not numerically feasible, to perform FEM with all structures described in the highest  
118 detail. On the other hand, it is difficult to decide beforehand how precise the morphologic  
119 model needs to be. Therefore, we think it is important to first have a high-resolution  
120 morphologic model available, which can then be simplified to the modeler's judgment.

121

122 In the current paper we provide these high-quality models by combining data originating  
123 from two different tomographic techniques: State-of-the-art  $\mu$ CT tomography allows to  
124 obtain precise data on bony structures, but due to the low X-ray absorption of soft tissue, CT  
125 generates poor quality images of soft tissue (Lemmerling et al., 1997). Therefore we  
126 combine these data with measurements from another and relatively new technique:  
127 Orthogonal-plane fluorescence optical-sectioning (OPFOS) microscopy or tomography. This  
128 method images both bone and soft tissue at the same time and in high-resolution.

129

130 As gerbil is one of the standard laboratory animal models in fundamental hearing research,  
131 we chose this species for our first model.

132

133

## 134 MATERIALS and METHODS

135

### 136 Dissection

137 All animal manipulations in this work were performed in accordance with Belgian  
138 legislation and the directives set by the Ethical committee on Animal Experimentation of our  
139 institution (University of Antwerp, Belgium). Three adult Mongolian gerbils (*Meriones*  
140 *unguiculatus*), aged between three and six months, were used. They were housed in cages  
141 with food and water ad libitum in our animal facility.

142

143 The animals were euthanized using carbon dioxide, followed by a cardiac perfusion with  
144 physiological fluid to rinse out all the blood from the gerbil head blood vessels. This step is  
145 necessary to allow for OPFOS tomography (as we will explain below). The gerbils are then  
146 decapitated and the right temporal bones were isolated. The specimens were reduced in size  
147 until only the bulla was left containing the middle and inner ear, cf. Figure 1. During the  
148 harvesting of these bullas, continuous moistening with mist from an ultrasonic humidifier  
149 (Bionaire BT-204) was applied to avoid dehydration.

150

151

### 152 Cross sectional imaging of bone with X-ray tomography

153 The first stage of 3D tomographic recording of the ME was achieved using micro-scale  
154 X-ray computed tomography. The dissected bullae were enclosed in separate Eppendorf  
155 vials, together with a calibration object and a few droplets of physiological fluid at the  
156 bottom. In this way a 100% saturated humid environment was created to avoid dehydration  
157 artifacts. Another droplet of fluid was placed in the ear canal – which could help – to  
158 distinguish the outline border of the TM shape with the air-filled ME cavity. Water and air  
159 have a slightly different X-ray absorption coefficient, so a layer of water on the extremely  
160 thin TM can help to reveal its medial shape outline. In previous work, we measured the  
161 shape of the eardrum before and after putting fluid on the membrane: even with a 10 mm  
162 water column in the ear canal, no measurable deformation was found with moiré  
163 profilometry of 15  $\mu\text{m}$  resolution (Buytaert et al., 2009). As the droplet of water is less than 3  
164 mm high (inducing a pressure load of 30 Pa) the TM deformation is well below the  $\mu\text{CT}$   
165 measurement resolution. The Eppendorf vials (made from polypropylene) are almost X-ray  
166 transparent. Especially bone absorbs X-rays well, thus creating a high contrast in  
167 transmission recordings. The small calibration objects were custom-made from polyvinyl  
168 chloride (PVC) in our mechanical workshop and possess about the same X-ray absorption  
169 properties as thin bone (Gea et al., 2005). They served as an independent calibration to  
170 verify the  $\mu\text{CT}$  device specifications.

171

172 The vials containing gerbil specimens were scanned at the UGCT scanning facility at Ghent  
173 University ([www.ugct.ugent.be](http://www.ugct.ugent.be)) using a custom-built  $\mu\text{CT}$  scanner of medium energy (up to  
174 160 keV). The scanner has a directional X-ray tube with a feature recognition capability up to

175 2  $\mu\text{m}$  (Masschaele et al., 2007). The scans were performed at a tube voltage of 120 kV  
176 (photon energy levels ranging from 0 to 120 keV) and a current of 58  $\mu\text{A}$ . A custom-made vial  
177 holder was mounted on a computer-controlled rotation table (MICOS, UPR160F-AIR). For  
178 each specimen a series of 1000 shadow projections of 1496x1880 pixels was recorded  
179 covering an object rotation of 360 degrees (or one recording every 0.36 degrees).  
180 Reconstruction of the tomographic data volume to serial sections was achieved using the  
181 back-projection algorithms of the Octopus software package (Dierick et al., 2004), resulting  
182 in 1780 reconstructed cross sections of 1496x1496 pixels. From these calculated cross  
183 sections with an isometric pixel size of 8.5  $\mu\text{m}$ , accurate 3D models of the three ossicles and  
184 other bony structures were generated. All three datasets cover a volume of 15.1 x 12.7 x  
185 12.7 mm (1780x1496x1496 times 8.5  $\mu\text{m}$ ).

186

187

#### 188 Cross sectional imaging of soft tissue with optical tomography

189 Due to the low X-ray absorption of soft tissue, another tomographic technique was  
190 needed: orthogonal-plane fluorescence optical-sectioning microscopy or OPFOS (Voie et al.,  
191 1993). OPFOS was initially developed to image the inner ear cochlea, but it has also been  
192 used in ME studies (Voie, 2002; Buytaert and Dirckx, 2007; 2009). In the OPFOS method,  
193 parallel optical sections through a macroscopic biomedical specimen are created by means  
194 of a thin sheet of laser light, and the fluorescence originating from within the cross section of  
195 the light sheet with the tissue is recorded in the direction perpendicular to the plane of the  
196 laser light. The light emitted by the specimen originate from auto-fluorescence or from  
197 staining the specimen with a fluorescent dye. OPFOS images both bone and soft tissue at the  
198 same time and in real-time, as no (back-projection) calculations are required. It allows  
199 region-of-interest (ROI) imaging and has both a high sectioning and a high in-plane  
200 resolution. Hence, perfectly and automatically aligned images of virtual cross sections can be  
201 obtained. OPFOS scanning was performed at the Laboratory of BioMedical Physics at the  
202 University of Antwerp ([www.ua.ac.be/bimef](http://www.ua.ac.be/bimef)) with a custom-built setup using bi-directional  
203 light-sheet illumination (Buytaert and Dirckx, 2009; Buytaert, 2010).

204

205 For OPFOS imaging, an elaborate specimen preparation is needed (Voie, 2002; Buytaert and  
206 Dirckx, 2009), as the technique requires the specimens to be perfectly transparent. Before

207  $\mu$ CT scanning, all blood was removed from the blood vessels, as coagulated blood cannot be  
208 made transparent afterwards. After  $\mu$ CT recording, a 10% neutral buffered Formalin bath  
209 was applied. Next, all calcium was removed using 10% EDTA in water solution combined with  
210 microwaves. Because of this decalcification, the OPFOS method has to be performed second  
211 after  $\mu$ CT X-ray scanning. Then, the specimens were dehydrated using a slowly graded  
212 ethanol series, up till 100%. Next, all tissue was refractive index matched using a slowly  
213 graded Spalteholz fluid series, again up till 100%. As a result, the specimens become entirely  
214 transparent when submerged in pure Spalteholz fluid. Finally, to obtain stronger  
215 fluorescence, the specimens are stained with Rhodamine B.

216

217 Both soft tissue and bone were made transparent and fluorescent; hence, both tissue types  
218 are visualized with the technique. We focused on region-of-interest (ROI) OPFOS imaging of  
219 ME ligaments, tendons and muscles, while images of the (often larger) bony structures are  
220 more easily obtained from  $\mu$ CT. Comparison of high-resolution  $\mu$ CT and OPFOS data allows  
221 us to distinguish bone from soft tissue in the OPFOS data. Merging of the two datasets  
222 generates the complete ME model with all of its functional components accounted for.

223

224 The shape of the TM was obtained from the  $\mu$ CT data. The OPFOS technique is able to  
225 visualize this extremely thin tissue when performing ROI imaging on a small part of the  
226 membrane, cf. Figure 2. However, to image the membrane full-field with OPFOS, one needs  
227 to zoom out and the resolution needed to adequately visualize this thin membrane is lost.  
228 Furthermore, the eardrum is prone to preparation artifacts: Because the gerbil specimens  
229 went through an extensive procedure of tissue fixation, decalcification, dehydration and  
230 Spalteholz treatment, the extremely thin TM can get deformed. Therefore, the data on  
231 eardrum shape are obtained from the CT images, recorded before any specimen processing  
232 was applied. X-rays are normally not suited to image soft tissue, especially if it is very thin,  
233 like the eardrum. We tried to counter this problem by applying a droplet of physiological  
234 fluid through the ear canal on top of the membrane. The medial border of the droplet and  
235 eardrum then become more easily distinguishable from air in the ME cavity. In this way, the  
236 membrane outline will be obtained without deformation and with adequate resolution.

237

238 Apart from the specimen preparation, the OPFOS method has another disadvantage as it

239 suffers from stripe artifacts. Opaque regions or areas of less transparency locally reduce the  
240 intensity of the laser light sectioning sheet, causing shadow lines or stripes in the rest of the  
241 image. This is partially countered by simultaneous dual light sheet illumination in our setup  
242 (Buytaert and Dirckx, 2009).

243

244 Measuring and analyzing the OPFOS data is very time-consuming; therefore, only one gerbil  
245 ear has been processed. On the other hand, the  $\mu$ CT data of all three gerbils was analyzed.

246

247

248 Visual observations

249 We performed visual observations of the orientation, location, shape and suspension  
250 of the ossicular chain inside opened ME bullae with an operating microscope (Zeiss, OPMI  
251 Sensera S7). When 3D computer data, models and results were obtained from  $\mu$ CT or OPFOS  
252 with striking features, they were compared to qualitative observations of the real geometry  
253 in opened bullae with the operating microscope to verify their interpretation. These  
254 experiences gave us the necessary expertise to confirm the 3D model results and conclusions  
255 of the present paper. For instance, after a targeted dissection we could visually confirm that  
256 the posterior incudal ligament in gerbil indeed exists as one whole band instead of two  
257 separate structures, as we found in our OPFOS data and model.

258

259

260 3D segmentation and reconstruction

261 After obtaining several series of object cross sections – one  $\mu$ CT set originating from  
262 back projection calculations, and several ROI datasets from direct OPFOS recordings – we  
263 identified and segmented the relevant structures in all images. The goal of segmentation is  
264 to locate objects boundaries, which in turn allows software to build 3D surface meshes by  
265 triangulation.

266

267 In our case, segmentation was done manually for thousands of sections using the  
268 commercial image segmentation and three-dimensional surface mesh generating software  
269 package Amira 5.3 (Visage Imaging). Manual segmentation might seem primitive and time-  
270 consuming; but using our morphological expertise, manual segmentation delivers better  
271 results than purely automated segmentation based on thresholding of gray scale values. The



272 Amira software package uses the marching cubes algorithm for triangulation. It takes eight  
273 neighboring voxel locations at a time (forming an imaginary cube), after which the  
274 polygon(s) needed to represent the part of the isosurface that passes through this cube are  
275 determined. The individual polygons are finally fused into the intended surface. This leads to  
276 subvoxel triangulation that easily manages sharp angles. When smoothing or simplification  
277 (reduction of the number of triangles) is used, the program takes the 'steepness' of the  
278 surface into account: Flat surface parts are more reduced than curved parts.

279

280 As final result, we end up with triangulated surface meshes for the  $\mu$ CT and OPFOS datasets.  
281 These can be further developed into finite-element volume meshes using Amira or other  
282 packages. On the website of the Laboratory of BioMedical Physics group we suggest some  
283 powerful and open-source volume generating software, e.g. PreView.

284

285

#### 286 Merging of CT and OPFOS models

287 All cross sections in a  $\mu$ CT dataset, and therefore all models of ME components  
288 originating from it, are inherently perfectly aligned within the data stack. The OPFOS  
289 datasets were focused on the soft tissue by separate ROI recordings. However, parts of the  
290 bone are included in the OPFOS ROI recordings as well. The cross sections within each ROI  
291 OPFOS data stack are also perfectly aligned, but the resulting mesh models per stack are  
292 unrelated to the other OPFOS datasets (because of different ROI zooming and/or other  
293 slicing orientation) and unrelated to the CT dataset and models.

294

295 To merge the OPFOS data with the  $\mu$ CT data, the  $\mu$ CT dataset was used as a reference. We  
296 did not merge the 2D image cross sections, but the 3D mesh models: All partial bone models  
297 from ROI OPFOS were three-dimensionally aligned to corresponding parts of the  $\mu$ CT models  
298 using an iterative spatial transformation least-squares minimization process of the Amira  
299 software package. This process uses the Iterative Closest Point (ICP) algorithm to minimize  
300 the difference between two point clouds (e.g. all surface nodes of respectively an OPFOS and  
301 a  $\mu$ CT mesh model). ICP iteratively revises the spatial transformation (6 degrees of freedom  
302 for translation and rotation) needed to minimize the Euclidean distance between the points  
303 of two datasets. This concept is referred to as the Procrustes superimposition method: The

304 root-mean-square (RMS) of the distances between corresponding points of the two surfaces  
305 are evaluated. Corresponding point pairs are created by finding the closest point of the  
306 reference ( $\mu$ CT) surface mesh for *each* point of the other (OPFOS) surface mesh. When the  
307 two surfaces are identical and perfectly superimposed, the RMS of all corresponding point  
308 distances will be zero. In the case of the OPFOS versus the  $\mu$ CT stapes model for instance, we  
309 obtained a root-mean-square difference of 17  $\mu$ m (or two  $\mu$ CT voxels). After obtaining such a  
310 good match between the OPFOS and  $\mu$ CT bone model, we applied the same spatial  
311 transformation to the OPFOS soft tissue mesh(es) from that OPFOS dataset. In this way, all  
312 OPFOS datasets were combined with  $\mu$ CT data into one model.

313

314

## 315 RESULTS

316

### 317 Computed tomography

318 Three gerbil ears were recorded with  $\mu$ CT, delivering three isometric data stacks of  
319 reconstructed cross sections (pixel size 8.5x8.5  $\mu$ m, separated 8.5  $\mu$ m). To illustrate the  
320 image quality, we present one  $\mu$ CT cross section in Figure 3. Full movies of all cross sections  
321 are available on our website and the entire dataset is available upon request. Notice how  
322 distinguishable the ossicle boundaries, the incudomalleolar and incudostapedial joint cleft and  
323 the annular ligament cleft are in the figure. This high contrast and resolution facilitates the  
324 segmentation process considerably.

325

326 Our main attention went to the ME; but separate 3D surface meshes were also created of  
327 the fluid-filled bony labyrinth of the inner ear (cochlea scalae and modiolus, and vestibular  
328 apparatus), cf. Figure 1 and Figure 4. The ME bulla air cavities of all gerbils are modeled as  
329 well. They give an indication of the enclosed air volume in the ME, cf. Table 1. These  
330 segmented volumes include the volume of the ossicles, ligaments and muscles. Finally, a  
331 separate rudimentary mesh of all bone using a fixed segmentation threshold was made.  
332 Using transparent rendering for this large model, one can virtually look inside the bulla and  
333 observe the ossicles and inner ear inside, cf. Figure 1. We listed volume, dimensions and  
334 several other properties of the ossicles, the TM and the ME bulla cavity in Table 1 to Table 3.  
335 These and other quantitative data is readily and accurately available from our models.

336 The mass of malleus, incus and stapes are respectively 1.145 mg, 0.633 mg and 0.116 mg as  
337 reported by Nummela, 1995. Adopting these representative values for our specimen in  
338 combination with the volumes given in Table 1, we get an average ossicle bone density of  
339  $1.37 \times 10^3 \text{ kg/m}^3$  for the stapes and  $1.74 \times 10^3 \text{ kg/m}^3$  for incus and malleus.

340

341 Note that the outline of the TM was surprisingly but successfully visualized using  $\mu$ CT. The  
342 resolution was just high enough to show the shape outline of the extremely thin membrane.  
343 Thickness information could not be obtained. Using a fluid droplet in the ear canal to aid in  
344 distinguishing the medial border of the eardrum partially failed, as can be seen in Figure 3:  
345 Fluid is not covering the entire membrane surface in the ear canal because of an air bubble.

346

347 Finally, we could observe channels (blood vessels) inside the ossicles, occurring especially in  
348 the incus and malleus bone, cf. Figure 5. The ossicular surface shapes are almost identical  
349 between all three animals, and the same is true for the size, volume and branching layout of  
350 the major channels inside them.

351

352

### 353 OPFOS tomography

354 We will now discuss all identified (soft) tissue structures of the ME of gerbil 2,  
355 measured with OPFOS.

356

#### 357 *Posterior incudal ligament*

358 Using  $\mu$ CT, the posterior incudal ligament cannot be found, cf. Figure 6A-B, while using  
359 OPFOS it is clearly visible, cf. Figure 6C-E. This comparison between the two tomographic  
360 imaging techniques clearly demonstrates the usefulness of combining the two methods.

361

362 After segmentation and 3D representation, cf. Figure 6F-G, one can see that the ligament is  
363 built as one whole part and forms one sickle-shaped band of fibrous tissue. Its tiny volume  
364 amounts to  $0.013 \text{ mm}^3$ . The sickle has its smallest thickness (orthogonally to the image plane  
365 of Figure 6F) of  $42 \mu\text{m}$  near the incus short process and broadens to  $190 \mu\text{m}$  towards the  
366 bulla edge. The contact area at the middle-ear cavity wall is also a bit larger than the contact  
367 area on the incus crus.

368

369

*Anterior malleal ligament*

370 The anterior process of the malleus has the shape of a (partially opened) hand-held Japanese  
371 folding fan, reaching towards the anterior bulla wall, cf. Figure 7 and Figure 8. The  
372 connective soft tissue of the anterior malleal ligament, which should connect the process to  
373 the bulla, is undistinguishable from bone, both in the OPFOS as in the CT recordings. This  
374 ligament is probably more ossified or cartilaginous than in some other species and no  
375 separate soft tissue model could be made.

376

377

*Superior malleal and incudal ligament and lateral malleal ligament*

378 According to real-time OPFOS observations, no superior malleal and incudal ligament are  
379 present in the gerbil ME, which is confirmed by visual observations with the operating  
380 microscope. In addition, no lateral malleal ligament could be discerned with either method.

381

382

*Tensor tympani muscle and tendon*

383 Figure 2A shows a high-resolution OPFOS section image through the tensor tympani muscle  
384 and tendon, the TM, the malleus' manubrium and the bulla. This image demonstrates  
385 OPFOS' capability to image bone and soft tissue in high-resolution.

386

387 After the segmentation and triangulation process, the volume of the tensor tympani muscle  
388 and tendon can be calculated from the obtained 3D model, and was found to be 0.486 mm<sup>3</sup>.  
389 The distance between the two most distant points on the combined structure is 3.25 mm.  
390 The diameter of the muscle tendon varies between 50-80 μm.

391

392 The cross-sectional area of a muscle (rather than volume or length) determines the amount  
393 of force it can generate. A first rough estimate of the order of magnitude of the maximum  
394 generated force of the muscle can be derived as follows. By dividing the muscle belly volume  
395 by an average muscle fiber length of 400 μm (estimated from the OPFOS images), we end up  
396 with a cross sectional area of  $1.2 \times 10^{-2}$  cm<sup>2</sup>. A common conversion factor from this area to  
397 the maximal isometric contraction force is given by 25 N/cm<sup>2</sup> for skeletal muscle (Nigg and  
398 Herzog, 1999), giving a maximally generated force of this muscle of 0.3 N. An interesting  
399 comparison of the effect of this force on the malleus can be made by translating this number

400 into a corresponding static pressure working on the TM from the ear canal side. Dividing the  
401 force of 0.3 N by the (projected) area of the pars tensa of the TM of gerbil 2 (13.64 mm<sup>2</sup>, cf.  
402 Table 2), we obtain a (maximum) static pressure of 22 kPa. The magnitude of this pressure  
403 falls in the range of static pressures associated with scuba diving or taking an airplane.

404

405 The final merged 3D model shows that the tensor tympani muscle belly is larger than  
406 expected from visual observations. Its main part is hidden as it is situated in a gap between  
407 the spiraled cochlear dome and the bulla wall.

408

#### 409 *Stapedial artery*

410 A typical anatomical feature of the gerbil ME is the stapedial artery running through a bony  
411 channel on the surface of the first cochlear turn and passing through the stapes crura in the  
412 ME air cavity. Using OPFOS, it was possible to image this relatively large stapedial artery, cf.  
413 Figure 9. We could even distinguish and separately model the stapedial artery soft tissue  
414 wall (the actual blood vessel) and its fluid-filled lumen.

415

416 The diameter of the blood vessel was the smallest in between the crura and amounted to  
417 355 μm with (i.e. outer diameter) and 275 μm without (i.e. inner diameter) the blood vessel  
418 soft tissue wall. The wall had a thickness of about 40 μm.

419

#### 420 *Stapedius muscle and tendon*

421 After segmentation of the stapedius muscle and tendon, we end up with the mesh shown in  
422 Figure 9. The tiny volume enclosed in this (tendon & muscle) mesh amounts to 0.085 mm<sup>3</sup>  
423 and the two most distant points on the combined structure are 1.81 mm apart. The diameter  
424 of the tendon varies between 40-55 μm. If we again divide the volume by an estimated  
425 average muscle fiber length of 350 μm, we get a cross sectional area of  $2.4 \times 10^{-3}$  cm<sup>2</sup>.  
426 Multiplying this value by 25 N/cm<sup>2</sup> gives an estimation of 0.06 N for the maximum force the  
427 muscle can produce.

428

429 The merged 3D model shows that the stapedius muscle body is attached to the lateral  
430 (horizontal) semi-circular canal, cf. Figure 9. In the figure, a gap is seen between the semi-  
431 circular canal and the muscle because only the fluid-filled cavity of the canal is shown. When

432 showing bone as well, one sees the muscle clasps firmly around the lateral semi-circular  
433 canal wall.

434

#### 435 *Joint clefts*

436 As can be seen in Figure 2B, the incudomalleolar and incudostapedial joints can be easily  
437 distinguished on high-resolution OPFOS cross sections and appear to form a tight  
438 connection.  $\mu$ CT data also show both clefts, from which we made three-dimensional meshes.

439

440 The incudomalleolar joint connects the incus and malleus and has the shape of a twisted  
441 saddle. The gap or cleft between the ossicles could contain synovial fluid as it is considered a  
442 synovial joint; however, this is not confirmed from our OPFOS measurements nor  $\mu$ CT data  
443 in gerbil. No fluid or open space is detected in the joint cleft, and the joint seems quite rigid.  
444 This rigidity was already reported for other species by Guinan and Peake, 1967; Gundersen  
445 and Høgmøen, 1976. The thickness of the joint varies from nearly zero to 51  $\mu$ m. The gap or  
446 joint tissue is thinner at the lateral side.

447

448 The incudostapedial joint connects the incus lenticular process with the head of the stapes.  
449 Our model of this synovial joint shows an oval disk with an approximately even thickness of  
450 25.5  $\mu$ m. Again, the joint cleft seems to possess no synovial fluid and forms a rigid  
451 connection, which has also been reported in cat (Funnell et al., 2005).

452

453 OPFOS also visualized the stapedial annular ligament cleft in which the annular stapedial  
454 ligament is situated, forming a syndesmosis joint. A syndesmosis is a slightly movable  
455 articulation where bony surfaces are tightly united by a fibrous tissue ligament (Laurent,  
456 1998). The high resolution of the OPFOS data allows to make a 3D mesh of this thin  
457 structure, cf. Figure 10. The thickness of the ligament varies between 8 to 18  $\mu$ m, confirmed  
458 by the gap seen in the  $\mu$ CT cleft model which is about 12-18  $\mu$ m.

459

#### 460 *Chorda Tympani*

461 The chorda tympani nerve branches from the facial nerve and runs through the ME air  
462 cavity. In gerbil, the nerve jumps from a sort of support beam at the superior bulla wall to  
463 the malleus where it is tightly connected to the malleus neck in the vicinity of which the

464 tensor tympani muscle connects as well, cf. Figure 7. It hangs in the ME air space passing the  
465 incudal long process laterally and the manubrium medially. It rounds the malleus neck from  
466 the posterior to the anterior side, passing the tensor tympani tendon inferiorly. At the  
467 anterior side, it lies on the anterior process sheet until it disappears in a fissure of the bulla  
468 wall again. It was unexpected that the chorda tympani could be visualized so well in OPFOS  
469 cross sections, cf. Figure 8, because myelin nerve sheets can in principle not be made  
470 transparent by the Spalteholz process. Apparently, because the nerve is thin enough, the  
471 blurring effect of the less transparent chorda tympani was negligible.

472

473

#### 474 Merging of CT and OPFOS models

475 As described before, we obtained a series of cross sectional images from  $\mu$ CT with  
476 bone only, cf. Figure 3, and from OPFOS with bony and soft tissue structures, cf. Figure 2,  
477 Figure 6 and Figure 8. With OPFOS, we performed ROI recording of all soft tissue structures,  
478 so only incomplete parts of the ossicles were measured. However, using these partial models  
479 of ossicles and/or bulla bone that were recorded together with the soft tissue, we could  
480 align these bony structures (and thus the soft tissue structures as well) to the  $\mu$ CT bone  
481 models, cf. Figure 11, using the Procrustes superimposition method.

482

483 The merging and alignment of bony structures revealed that some shrinking of the gerbil 2  
484 specimen had occurred despite of our careful efforts during preparation. Using the warping  
485 procedure in Amira (similar to the Procrustes superimposition method, only allowing for  
486 scaling in every dimension as well), we found a shrinking factor of 8.4% in all three  
487 dimensions. After applying the spatial transformation and up-scaling, the OPFOS soft tissue  
488 meshes fit rather well in between the CT bone mesh models. For instance, corresponding  
489 bony parts of the malleus from OPFOS using a scale-factor of 8.4% were aligned with the  
490 malleus from  $\mu$ CT. After applying the same scaling and spatial transformation to the tensor  
491 tympani, its tendon attaches to the malleus, cf. Figure 11, and at the other side its muscle  
492 body inserts nicely in a bony cavity of the bulla of the inverse shape, cf. Figure 12. This and  
493 similar facts give us confidence in the merging of the data.

494

495

## 496 DISCUSSION

497

## 498 Imaging method

499 Several methods exist to measure and image the ME for the creation of FEM models.  
500  $\mu$ CT in itself is mainly suited to image the bony structures.  $\mu$ CT using contrast agents is a  
501 valuable alternative to our combined approach (Metscher, 2009). However, it is difficult to  
502 discriminate between bone and soft tissue, so it would be necessary to do  $\mu$ CT scans before  
503 and after staining, and merge the data as we now did with OPFOS. OPFOS offers a resolution  
504 down to 2 micrometer, which is seldom achieved in  $\mu$ CT. For this reason, we preferred  
505 OPFOS to obtain the soft tissue data. Multiple energy CT techniques have also proven to be a  
506 valuable method for discriminating between soft tissue and bone in CT images (Johnson et  
507 al., 2007; Granton et al., 2008). For large macroscopic structures the technique is indeed  
508 feasible, however, it becomes more difficult in the case of microscopic samples. The position  
509 of the micro-focus spot changes in an X-ray tube when its energy or source is altered. As a  
510 result, the datasets are slightly shifted in a complicated way, and tissue discrimination can  
511 no longer be done by simple subtraction or division. Gradually, these technical issues are  
512 being solved, so in the future dual-energy CT may be used to measure and discriminate soft  
513 tissue and bone.

514

515 The most used alternative to our method is conventional histological sectioning, which is  
516 unsurpassed in resolution and produces data on the bone and soft tissue simultaneously.  
517 Both the histological method as our combined method need a similar specimen preparation  
518 that can induce shrinking (Lane and Ráliš, 1983; Henson et al., 1994). Our method is  
519 considered non-destructive (as multiple measurements can be done on the sample) while  
520 histology can only measure the sample once and in one slicing orientation because of the  
521 need for physical cutting of the specimen. Furthermore, these 2D slices are often deformed  
522 during slicing, requiring difficult image processing and registration of all slices before  
523 generating a 3D model.  $\mu$ CT and OPFOS each deliver perfectly and automatically aligned  
524 cross sections that require no post-processing. Instead of registering every 2D slice, our  
525 method only needs to register complete 3D meshes of all submodels to one another. OPFOS  
526 further allows real-time virtual sectioning and imaging.

527



528

## 529 Human versus gerbil

530 When using animal models, it is important to be aware of the differences with human  
531 ME morphology. Figure 13 shows a schematic representation of all human ME components.  
532 In addition to the data prepared in this paper, we confirmed our findings in other gerbil ears  
533 during other studies using OPFOS and visual inspection with the operation microscope.

534

535 We found that in gerbil no superior incudal, no superior mallear and no lateral mallear  
536 ligament are present, contrary to the case in humans. The presence and/or function of  
537 superior attachments to malleus and incus as suspensory structures are of controversy,  
538 though many mathematical models or drawings of the human ME include such structures,  
539 cf. Table 2.1 in Mikhael, 2005; and Merchant and Nadol Jr., 2010.

540

541 It has been proposed by Rosowski et al., 1999 that the anterior mallear ligament is a bony  
542 connection to the bulla, while Elkhouri et al., 2006 observed the presence of some  
543 connective tissue. Our OPFOS measurements could not distinguish any soft tissue, and our  
544 CT measurement showed an ossified or cartilaginous connection. The anterior process also  
545 had a less pronounced shape in human than the Japanese fan-shaped structure in gerbil.

546

547 The posterior incudal ligament, which connects the incus short crus to the fossa incudes,  
548 exists in many different configurations, as is illustrated in Figure 14 by Funnell, 1972 (based  
549 on work by Kobayashi). From the OPFOS sections, cf. Figure 6C-E, the gerbil posterior  
550 ligament appears to fall in the category of human and cat configurations. However, it is only  
551 possible to appreciate the true configuration in 3D, cf. Figure 6F-G, which clearly places this  
552 gerbil ligament in the category of guinea pig and rabbit. The posterior incudal ligament  
553 consists of one sickle-shaped part. According to Sim and Puria, 2008, it has been observed  
554 that in human the two parts shown in Figure 14 are also connected around the tip of the  
555 short crus of the incus to form a single continuous ligament rather than two separate  
556 ligaments. In this respect, gerbil and human ME then would be alike.

557

558 We also found the chorda tympani nerve to be present in a special arrangement in gerbil,  
559 and more tightly connected to the malleus ossicle than in human: In human this nerve

560 traverses the open space of the ME cavity without actually attaching to the ossicles. In  
561 gerbil, there exists a tight connection with the malleus neck and the nerve lies on top of the  
562 Japanese fan-shaped anterior process sheet, cf. Figure 7 and Figure 8. Furthermore, the  
563 topographic relation of the chorda tympani to the tensor tympani muscle differs from  
564 human. In gerbil it runs hypotensoric (inferiorly to the tensor tympani) and in between the  
565 muscle and manubrium, as was confirmed in a recent publication by Ruf et al., 2009; while in  
566 human it passes epitensoric (superiorly to the tensor tympani), e.g. Maier, 2008.

567

568 We derived the ossicle bone density from our volume measurements and from mass data  
569 from literature. We obtained an ossicle bone density of  $1.37 \times 10^3 \text{ kg/m}^3$  for the stapes and  
570  $1.74 \times 10^3 \text{ kg/m}^3$  for incus and malleus. In comparison to human, the averaged malleus  
571 density is found to be  $2.31 \times 10^3 \text{ kg/m}^3$  and the averaged incus density is  $2.14 \times 10^3 \text{ kg/m}^3$   
572 (Sim and Puria, 2008). Another source mentions an average stapes density of  $2.2 \times 10^3 \text{ kg/m}^3$   
573 in human (Kirikae, 1960; Gan et al., 2004). Hence, gerbil ossicle densities appear to be  
574 significantly lower than in human.

575

576 Another contrast to human is that the stapedia artery is usually present in gerbil, while  
577 seldom in human.

578

579 Finally, our observations show that the gerbil manubrium of malleus is tightly fused over its  
580 full length with the TM, while in human it is mainly only fixed at the tip and lateral process of  
581 the manubrium (Koike et al., 2002).

582

583

#### 584 Resolution

585 We used state-of-the-art X-ray micro-computed tomography and the relatively new  
586 orthogonal-plane fluorescence optical-sectioning microscopy on the ME. In previous CT  
587 based studies of the ME, the following model resolutions were reported:  $5.5 \mu\text{m}$  on gerbil  
588 (Elkhouri et al., 2006),  $6 \mu\text{m}$  on human (Hagr et al., 2004),  $10 \mu\text{m}$  on cat (Decraemer et al.,  
589 2003) and  $10 \mu\text{m}$  on human (Vogel, 1999). Though these numbers are comparable to our  
590 isometric  $8.5 \mu\text{m}$  voxel size for  $\mu\text{CT}$  on gerbil bone, our data and models are of much higher  
591 quality than those shown in previous work. One reason might be that the previous authors

592 stated voxel size instead of resolution, while we actually achieve a true resolution of 8.5  $\mu\text{m}$ .  
593 Other factors such as scan parameter settings could also account for differences in image  
594 quality.

595  
596 ME soft tissue imaged with medical CT devices gave poor resolution (Lemmerling et al.,  
597 1997), and  $\mu\text{CT}$  delivered modest resolution (Sim and Puria, 2008). The same goes for MRI  
598 measurements of gerbil soft tissue structures, e.g. 45  $\mu\text{m}$  (Elkhouri et al., 2006). OPFOS is  
599 clearly better suited to achieve high-resolution sections on ligaments and muscles – with  
600 pixel sizes ranging from 1 to 5  $\mu\text{m}$  – as can be seen from our sections and 3D models, cf.  
601 Figure 2 and Figure 6 til Figure 11.

602  
603 The OPFOS method itself is little known but it was the first setup of the growing field now  
604 known as (Laser) Light Sheet based Fluorescence Microscopy (LSFM). The many different  
605 implementations and improvements of the technique have been listed in a review article by  
606 Buytaert et al., 2011. The construction of an OPFOS/LSFM setup is well feasible in the sense  
607 that all parts needed are readily available on the market. Researchers interested in the  
608 construction of such a setup or in collaboration are welcome to contact the authors, and  
609 even the first commercial devices are becoming available (Buytaert et al., 2011).

610

611

## 612 Artifacts

613 Segmentation of the fluid-filled inner ear channels in the  $\mu\text{CT}$  data showed that the  
614 round window in all three models is prominently bulged inwards toward the cochlea. This  
615 might indicate either a small overpressure in the ME air cavity or a loss of cochlear fluid  
616 because of dehydration or leakage.

617

618 Merging of OPFOS and  $\mu\text{CT}$  data revealed shrinking of the soft and bony tissue, most likely  
619 caused by the elaborate OPFOS specimen preparation (e.g. tissue fixation, decalcification,  
620 dehydration and Spalteholz treatment), though previous authors reported that this  
621 procedure induced negligible shrinking (Voie, 2002; Valk et al., 2005; Hofman et al., 2008).  
622 Thanks to the combination of OPFOS with  $\mu\text{CT}$ , we have undeformed reference data that we  
623 can use to derive a scaling factor. Homogeneous scaling with 8% of the OPFOS (bone and

624 soft tissue) models has partially corrected for the shrinking artifact. After decalcification of  
625 the sample, bone is reduced to a collagen matrix. The effect of decalcification cannot be  
626 investigated with  $\mu$ CT as all calcium is removed and X-ray absorption becomes negligible. It  
627 is, however, a reasonable assumption that dehydration will have a similar (and  
628 homogeneous) shrinking effect on both soft tissue and *decalcified* bone. In histology, the  
629 same specimen preparation (decalcification and dehydration) is performed and the same  
630 assumption (homogeneous shrinkage) is adopted.

631

632 Another artifact related to specimen preparation was noticed on the stapes. The footplate of  
633 the stapes is clearly convex and bulges inwards to the cochlea in the  $\mu$ CT models, e.g. Figure  
634 10. After decalcification, dehydration and Spalteholz treatment, the footplate of the OPFOS  
635 model showed some relaxation and shriveling of its convex shape. The models available for  
636 download therefore consist of  $\mu$ CT data for bone and OPFOS data for soft tissue meshes.

637

638 *Stripe* artifacts in OPFOS were strongly reduced but not entirely eliminated by our bi-  
639 directional illumination/sectioning OPFOS setup. In combination with manual segmentation,  
640 which also partially corrects for this artifact, no effect remained in the models so no image  
641 post-processing of the data was required.

642

643 OPFOS was not suited to image the TM, but the full-field outline of the TM shape was  
644 obtained from  $\mu$ CT: We could not measure a volume model of the TM with the correct  
645 thickness, but only a surface model. FEM modelers can, however, use the surface shape  
646 directly as a shell model, cf. Gan et al., 2004; Elkhouri et al., 2006; and apply either a uniform  
647 or a varying measured thickness distribution to their own choosing (as different approaches  
648 are taken by different modelers). Table 2 mentions average thickness data at three TM  
649 regions, measured on eleven gerbil TMs with confocal microscopy (Kuypers et al., 2005).

650

651

#### 652 Open source availability

653 All three-dimensional data and surface mesh models presented in this paper are  
654 freely available for educational and research purposes on the website of the Laboratory of  
655 BioMedical Physics: <http://www.ua.ac.be/bimef/models>.

656

657 Several educational and research 3D models have also been made available in the past  
658 (Eaton-Peabody Laboratory of Auditory Physiology, Ear & Auditory Research Laboratory,  
659 Auditory Mechanics Laboratory, Auditory Research Laboratory, OtoBiomechanics Group).

660

661

## 662 CONCLUSION

663

664 Finite-element computer modeling needs accurate three-dimensional models to obtain  
665 realistic simulation results for middle ear mechanics. 3D models are also useful in medical  
666 training or for the interpretation and presentation of experimental results. The middle ear  
667 does not only comprise the ossicles but also consists of soft tissue: tympanic membrane,  
668 ligaments, muscles, tendon and blood vessels.

669

670 In this paper, we presented an accurate and complete morphological 3D middle (and inner)  
671 ear model of gerbil. The model is freely available to the research community at our website.  
672 The presented model quality is unprecedented. The position, orientation and size of all  
673 components making up the gerbil middle ear are now accurately known and individually  
674 discussed.

675

676

## 677 ACKNOWLEDGEMENTS

678

679 We gratefully acknowledge the financial support of the Research Foundation – Flanders and  
680 the Fondation Belge de la Vocation. We thank Pieter Vanderniepen for his assistance in  
681 operating the CT device, Magnus Von Unge and Wim Decraemer for their feedback on  
682 human and gerbil anatomy, Fred Wiese for manufacturing the vial holder, Robert Funnell for  
683 the use of Figure 14, and Peter Aerts for feedback on muscle functionality.

684

685

686

687

## 688 REFERENCES

- 689 Beer H, Bornitz M, Hardtke H, Schmidt R, Hofmann G, Vogel U, Zahnert T, Huttenbrink K  
690 (2000) Modelling of components of the human middle ear and simulation of their dynamic  
691 behaviour. *Audiology and Neurotology* 4:156–162
- 692 Blayney A, Williams KR, Rice HJ (1997) A dynamic and harmonic damped finite element  
693 analysis model of stapedotomy. *Acta oto-laryngologica* 117:269-73
- 694 Buytaert JAN (2010) *New optical Tomographic & Topographic Techniques for Biomedical*  
695 *Applications*. University Press Zelzate.
- 696 Buytaert JAN, Aernouts J, Dirckx JJJ (2009) Indentation measurements on the eardrum with  
697 automated projection moiré profilometry. *Optics and Lasers in Engineering* 47:301-309
- 698 Buytaert JAN, Descamps E, Adriaens D, Dirckx JJJ (2011) The OPFOS microscopy family:  
699 High-resolution optical-sectioning of biomedical specimens. *Anatomical Research*  
700 *International* in press
- 701 Buytaert JAN, Dirckx JJJ (2007) Design and quantitative resolution measurements of an  
702 optical virtual sectioning three-dimensional imaging technique for biomedical specimens,  
703 featuring two-micrometer slicing resolution. *Journal of biomedical optics* 12:014039
- 704 Buytaert JAN, Dirckx JJJ (2009) Tomographic imaging of macroscopic biomedical objects in  
705 high resolution and three dimensions using orthogonal-plane fluorescence optical sectioning.  
706 *Applied optics* 48:941-918
- 707 Cheng T, Gan RZ (2008) Experimental measurement and modeling analysis on mechanical  
708 properties of tensor tympani tendon. *Medical engineering & physics* 30:358-66
- 709 Decraemer WF, Dirckx JJJ, Funnell WRJ (2003) Three-dimensional modelling of the middle-  
710 ear ossicular chain using a commercial high-resolution X-ray CT scanner. *Journal of the*  
711 *Association for Research in Otolaryngology : JARO* 4:250-63
- 712 Decraemer WF, Khanna SM, Dirckx JJJ (2002) The integration of detailed 3-dimensional  
713 anatomical data for the quantitative description of 3-dimensional vibration of a biological  
714 structure. An illustration from the middle ear. In E. P. Tomassini, ed. *Fifth International*  
715 *Conference on Vibration Measurements by Laser Techniques : Advances and Applications* ,  
716 p. 148-158.
- 717 Dierick M, Masschaele B, Hoorebeke LV (2004) Octopus, a fast and user-friendly  
718 tomographic reconstruction package developed in LabView®. *Measurement Science and*  
719 *Technology* 15:1366-1370
- 720 Eiber A, Freitag HG, Burkhardt C, Hemmert W, Maassen M, Rodriguez Jorge J, Zenner HP  
721 (2000) Dynamics of middle ear prostheses—simulations and measurements. *Audiology and*  
722 *Neurotology* 4:178–184

- 723 Elkhouri N, Liu H, Funnell WRJ (2006) Low-frequency finite-element modeling of the gerbil  
724 middle ear. *JARO-Journal of the Association for Research in Otolaryngology* 7:399–411
- 725 Funnell WRJ (1972) The Acoustical Impedance of the Guinea-Pig Middle Ear and the Effects  
726 of the Middle-Ear Muscles.
- 727 Funnell WRJ, Heng Siah T, McKee MD, Daniel SJ, Decraemer WF (2005) On the coupling  
728 between the incus and the stapes in the cat. *Journal of the Association for Research in*  
729 *Otolaryngology : JARO* 6:9-18
- 730 Funnell WRJ, Khanna SM, Decraemer WF (1992) On the degree of rigidity of the manubrium  
731 in a finite-element model of the cat eardrum. *The Journal of the Acoustical Society of*  
732 *America* 91:2082-2090
- 733 Funnell WRJ, Laszlo CA (1978) Modeling of the cat eardrum as a thin shell using the finite-  
734 element method. *The Journal of the Acoustical Society of America* 63:1461-1467
- 735 Gan RZ, Feng B, Sun Q (2004) Three-dimensional finite element modeling of human ear for  
736 sound transmission. *Annals of biomedical engineering* 32:847-59
- 737 Gan RZ, Reeves BP, Wang X (2007) Modeling of sound transmission from ear canal to  
738 cochlea. *Annals of biomedical engineering* 35:2180–2195
- 739 Gea SLR, Decraemer WF, Dirckx JJJ (2005) Region of interest micro-CT of the middle ear:  
740 A practical approach. *Journal of X-Ray Science and Technology* 13:137–147
- 741 Granton PV, Pollmann SI, Ford NL, Drangova M, Holdsworth DW (2008) Implementation of  
742 dual- and triple-energy cone-beam micro-CT for postreconstruction material decomposition.  
743 *Medical Physics* 35:5030
- 744 Guinan J, Peake WT (1967) Middle-Ear Characteristics of Anesthetized Cats. *The Journal of*  
745 *the Acoustical Society of America* 41:1237-1261
- 746 Gundersen T, Høgmoen K (1976) Holographic Vibration Analysis of the Ossicular Chain.  
747 81:16-25
- 748 Hagr AA, Funnell WRJ, Zeitouni AG, Rappaport JM (2004) High-Resolution X-Ray  
749 Computed Tomographic Scanning of the Human Stapes Footplate. *Journal of Otolaryngology*  
750 33:217–221
- 751 Henson MM, Henson OW, Gewalt SL, Wilson JL, Johnson GA (1994) Imaging the cochlea  
752 by magnetic resonance microscopy. *Hearing research* 75:75-80
- 753 Hofman R, Segenhout JM, Buytaert JAN, Dirckx JJJ, Wit HP (2008) Morphology and  
754 function of Bast's valve: additional insight in its functioning using 3D-reconstruction.  
755 *European archives of oto-rhino-laryngology* 265:153-157
- 756 Johnson TRC, Krauss B, Sedlmair M, Grasruck M, Bruder H, Morhard D, Fink C, Weckbach  
757 S, Lenhard M, Schmidt B, Flohr T, Reiser MF, Becker CR (2007) Material differentiation by  
758 dual energy CT: initial experience. *European radiology* 17:1510-1517

- 759 Kirikae I (1960) *The Structure and Function of the Middle Ear*. University of Tokyo Press.
- 760 Koike T, Wada H, Kobayashi T (2002) Modeling of the human middle ear using the finite-  
761 element method. *The Journal of the Acoustical Society of America* 111:1306-17
- 762 Kuypers LC, Dirckx JJJ, Decraemer WF, Timmermans J-P (2005) Thickness of the gerbil  
763 tympanic membrane measured with confocal microscopy. *Hearing research* 209:42-52
- 764 Ladak HM, Funnell WRJ (1996) Finite-element modeling of the normal and surgically  
765 repaired cat middle ear. *The Journal of the Acoustical Society of America* 100:933
- 766 Lane J, Ráliš Z (1983) Changes in dimensions of large cancellous bone specimens during  
767 histological preparation as measured on slabs from human femoral heads. *Calcified Tissue*  
768 *International* 35:1-4
- 769 Laurent C (1998) The action of hyaluronan on repair processes in the middle ear In C.  
770 Laurent, ed. *The chemistry, biology and medical applications of hyaluronan and its*  
771 *derivatives* Portland, p. 283-289.
- 772 Lee C-F, Chen P-R, Lee W-J, Chen J-H, Liu T-C (2006) Computer Aided Three-Dimensional  
773 Reconstruction and Modeling of Middle Ear Biomechanics By High-Resolution Computed  
774 Tomography and Finite Element Analysis. *Biomedical Engineering: Applications, Basis and*  
775 *Communications* 18:214
- 776 Lee DH, Chan S, Salisbury C, Kim N, Salisbury K, Puria S, Blevins NH (2010)  
777 Reconstruction and exploration of virtual middle-ear models derived from micro-CT datasets.  
778 *Hearing Research* 263:198-203
- 779 Lemmerling MM, Stambuk HE, Mancuso a a, Antonelli PJ, Kubilis PS (1997) CT of the  
780 normal suspensory ligaments of the ossicles in the middle ear. *AJNR. American journal of*  
781 *neuroradiology* 18:471-7
- 782 Lord RM, Abel EW, Mills RP (1999) A Finite Element Model of the Middle Ear In  
783 *Proceedings of NAFEMS WORLD CONGRESS '99 on Effective Engineering Analysis* , p.  
784 487-494.
- 785 Maier W (2008) Epitensoric Position of the Chorda Tympani in Anthroidea: a New  
786 Synapomorphic Character, with Remarks on the Fissura Glaseri in Primates In E. J. Sargis &  
787 M. Dagosto, eds. *Mammalian Evolutionary Morphology* Dordrecht: Springer, p. 347-360.
- 788 Masschaele B, Cnudde V, Dierick M, Jacobs P, Vanhoorebeke L, Vlassenbroeck J (2007)  
789 UGCT: New X-ray radiography and tomography facility. *Nuclear Instruments and Methods in*  
790 *Physics Research Section A: Accelerators, Spectrometers, Detectors and Associated*  
791 *Equipment* 580:266-269
- 792 Merchant SN, Nadol Jr. JB (2010) *Schucknect's Pathology of the Ear*. PMPH-USA.
- 793 Metscher BD (2009) MicroCT for comparative morphology: Simple staining methods allow  
794 high-contrast 3D imaging of diverse non-mineralized animal tissues. *BMC Physiology* 9:1-14



- 795 Mikhael CS (2005) Finite element model of the human middle ear. :120
- 796 Mikhael CS, Funnell WRJ, Bance M (2004) Middle-ear finite-element modelling with  
797 realistic geometry and a priori material-property estimates In 28th Ann Conf Can Med Biol  
798 Eng Soc , p. 126-129.
- 799 Nigg BM, Herzog W (1999) Biomechanics of the musculo-skeletal system 2nd ed. Wiley.
- 800 Nummela S (1995) Scaling of the mammalian middle ear. *Hearing research* 85:18–30
- 801 Prendergast P, Ferris P, Rice HJ, Blayney A (2000) Vibro-acoustic modelling of the outer and  
802 middle ear using the finite-element method. *Audiology and Neurotology* 4:185–191
- 803 Puria S, Steele CR (2010) Tympanic-membrane and malleus-incus-complex co-adaptations  
804 for high-frequency hearing in mammals. *Hearing Research* 263:183–190
- 805 Rodt T, Ratiu P, Becker H, Bartling S, Kacher D, Anderson M, Jolesz F, Kikinis R (2002) 3D  
806 visualisation of the middle ear and adjacent structures using reconstructed multi-slice CT  
807 datasets, correlating 3D images and virtual endoscopy to the 2D cross-sectional images.  
808 *Neuroradiology* 44:783–790
- 809 Rosowski JJ, Ravicz ME, Teoh SW, Flandermeyer D (1999) Measurements of middle-ear  
810 function in the Mongolian gerbil, a specialized mammalian ear. *Audiology & neuro-otology*  
811 4:129-136
- 812 Ruf I, Frahnert S, Maier W (2009) The chorda tympani and its significance for rodent  
813 phylogeny. *Mammalian Biology - Zeitschrift fur Saugetierkunde* 74:100-113
- 814 Sim JH, Puria S (2008) Soft Tissue Morphometry of the Malleus–Incus Complex from Micro-  
815 CT Imaging. *JARO-Journal of the Association for Research in Otolaryngology* 9:5–21
- 816 Sun Q, Gan RZ, Chang K-H, Dormer KJ (2002) Computer-integrated finite element modeling  
817 of human middle ear. *Biomechanics and modeling in mechanobiology* 1:109-122
- 818 Valk WL, Wit HP, Segenhout JM, Dijk F, Want JJJ van der, Albers FWJ (2005) Morphology  
819 of the endolymphatic sac in the guinea pig after an acute endolymphatic hydrops. *Hearing*  
820 *research* 202:180-7
- 821 Vogel U (1999) New approach for 3D imaging and geometry modeling of the human inner  
822 ear. *ORL* 61:259–267
- 823 Voie AH (2002) Imaging the intact guinea pig tympanic bulla by orthogonal-plane  
824 fluorescence optical sectioning microscopy. *Hearing research* 171:119-128
- 825 Voie AH, Burns DH, Spelman FA (1993) Orthogonal-plane fluorescence optical sectioning:  
826 three-dimensional imaging of macroscopic biological specimens. *Journal of microscopy*  
827 170:229-236

828 Wada H, Metoki T, Kobayashi T (1992) Analysis of dynamic behavior of human middle ear  
829 using a finite-element method. The Journal of the Acoustical Society of America 92:3157-  
830 3168

831 Wang H, Northrop C, Burgess B, Liberman MC, Merchant SN (2006) Three-dimensional  
832 virtual model of the human temporal bone: a stand-alone, downloadable teaching tool.  
833 Otology & neurotology: official publication of the American Otological Society, American  
834 Neurotology Society [and] European Academy of Otology and Neurotology 27:452

835

836

837 REFERENCES to WEBSITES with MODELS

838

839 Eaton-Peabody Laboratory of Auditory Physiology: '3D Virtual Models of the Human  
840 Temporal Bone and Related Structures'

841 <http://research.meei.harvard.edu/Otopathology/3dmodels/download.html>

842

843 Auditory Research: 'The Vertebrate Ear and Temporal Bone'

844 [http://cbaweb2.med.unc.edu/henson\\_mrm/](http://cbaweb2.med.unc.edu/henson_mrm/)

845

846 Auditory Mechanics Laboratory: '3D Ear Human Ear'

847 <http://audilab.bmed.mcgill.ca/~daren/3Dear/>

848

849 Ear & Auditory Research Laboratory: '3D Overview of Ear Anatomy'

850 <http://ear-lab.medicine.dal.ca/3D/3D-Overview.htm>

851 OtoBiomechanics Group: microCT data and 3D reconstructions

852 <http://www.stanford.edu/~puria1/Site/Imaging.html>

853

854

855

856

857

858

859

860

861

862

## 863 TABLE CAPTIONS

864

865 *Table 1: Volume, surface area and number of triangles for gerbil 1 (G1), gerbil 2 (G2) and*  
866 *gerbil 3 (G3) ear components, derived from the 3D surface meshes obtained from  $\mu$ CT. The*  
867 *ME cavity volume incorporates the air, ossicles and ME soft tissue volume.*

868

869

870 *Table 2: Geometry parameters of the TM for gerbil 1 (G1), gerbil 2 (G2) and gerbil 3 (G3) ear*  
871 *components, derived from the 3D surface meshes obtained from  $\mu$ CT.*

872 *(\*Mean thickness data from confocal microscopy on 11 gerbils by Kuypers et al., 2005.)*

873

874

875 *Table 3: 3D length of the manubrium (umbo tip till lateral process tip, cf. figure 5) and 3D*  
876 *height of the stapes (medial footplate till tip stapes head) for gerbil 1 (G1), gerbil 2 (G2) and*  
877 *gerbil 3 (G3), derived from the 3D surface meshes obtained from  $\mu$ CT.*

878

879

880

881

882

883

884

885

886

887

888

889

890

891

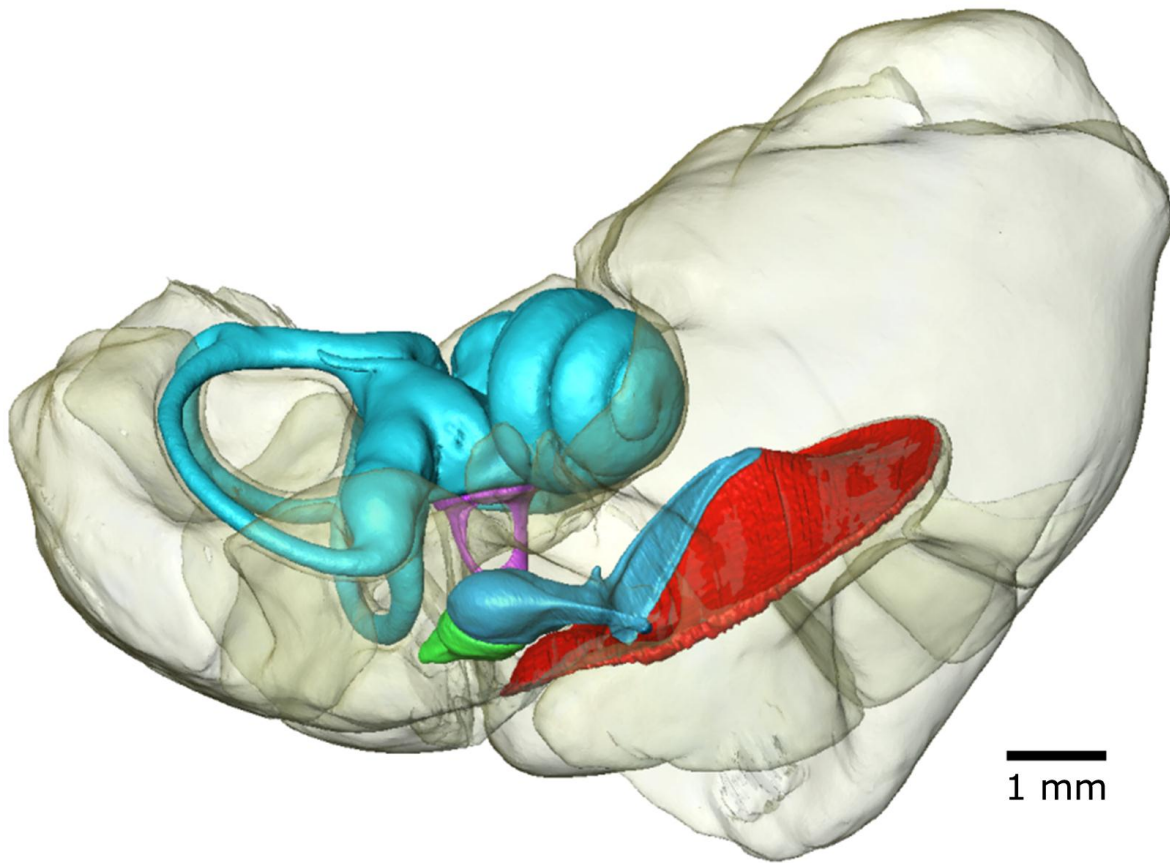
892

893

894

895 FIGURES

896

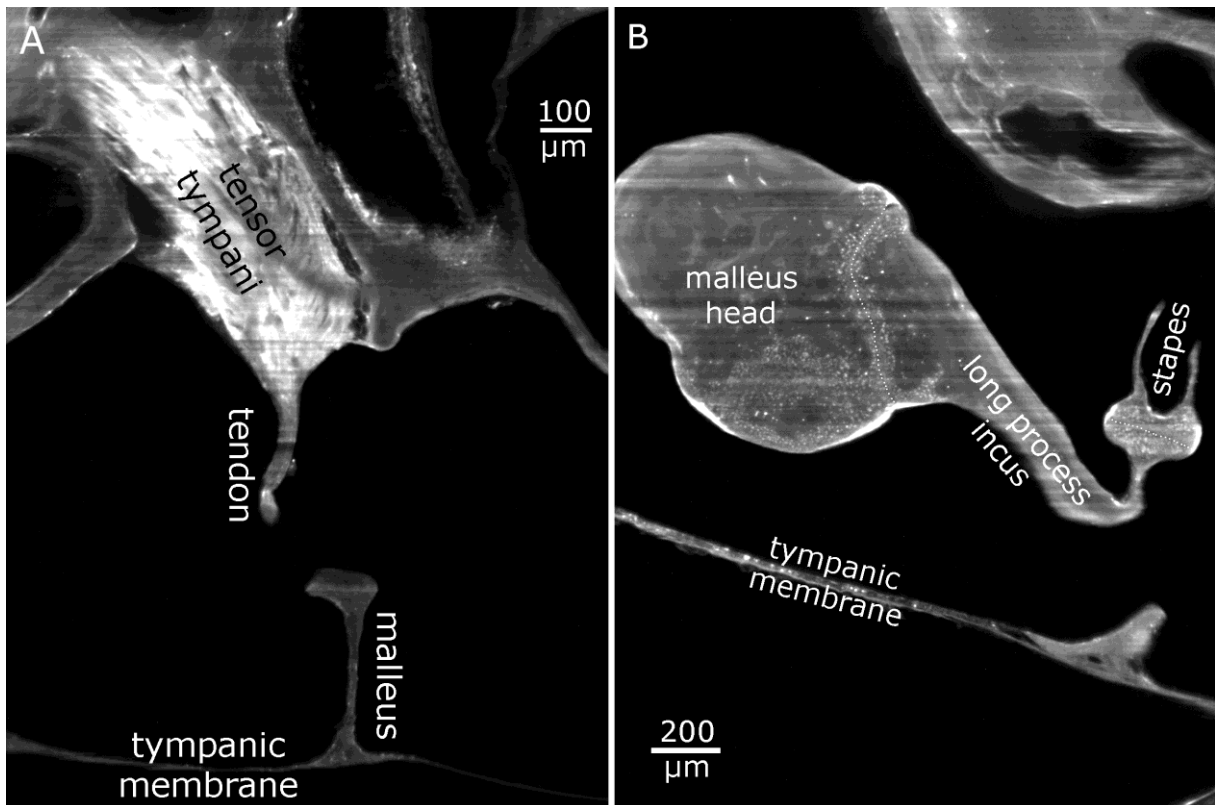


897

898 Figure 1: 3D model of separate surface meshes of bony middle and inner ear components of

899 gerbil 2, obtained from  $\mu$ CT. The bulla is rendered transparent. Voxel size  $8.5 \times 8.5 \times 8.5 \mu\text{m}$ .

900



901

902

903

904

905

906

907

908

909

910

911

912

913

914

915

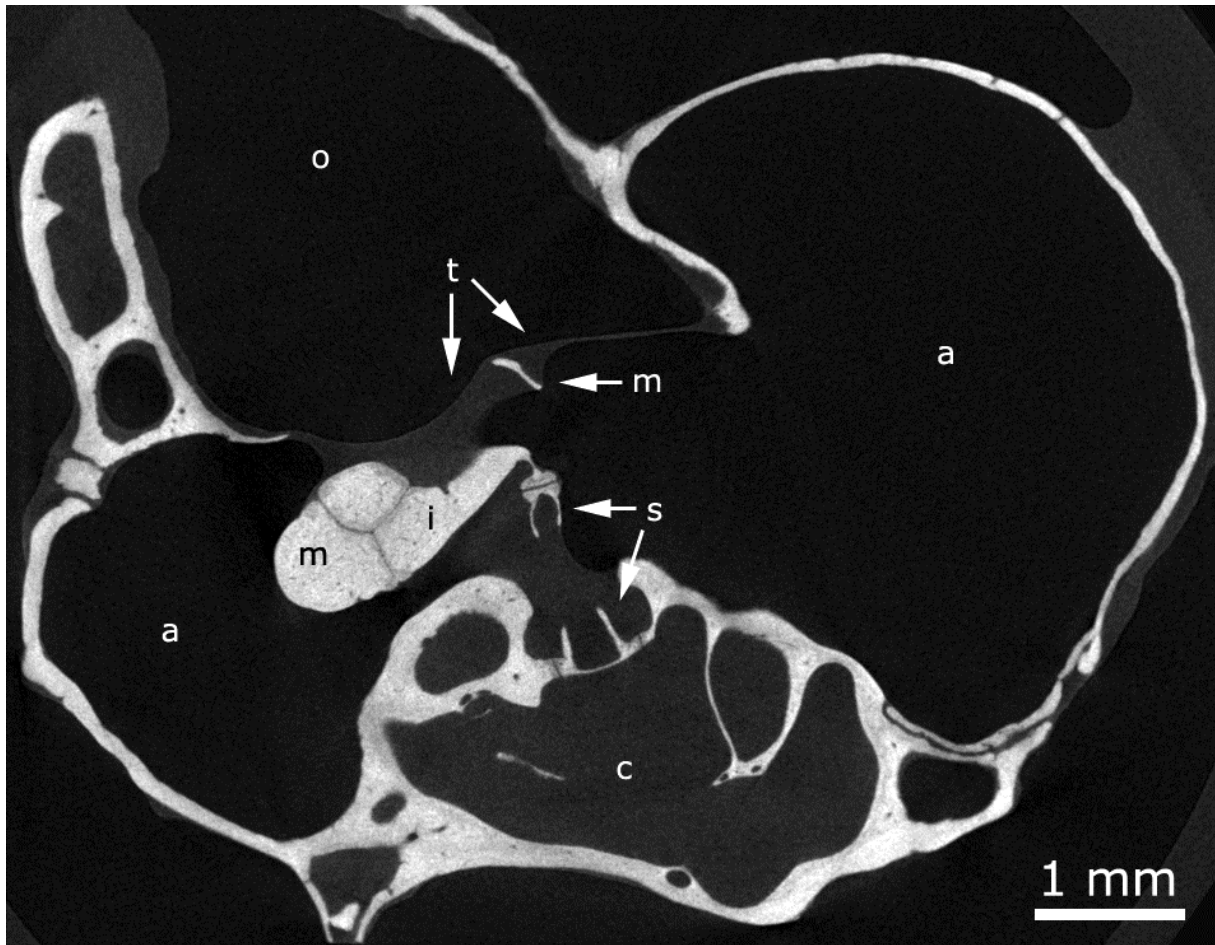
916

917

918

Figure 2: 2D virtual cross sections delivered by the OPFOS technique. A) Tensor tympani tendon reaching down towards malleus. B) Incudomalleolar and incudostapedial articulation.

Pixel size 1.5x1.5 μm.



919

920 Figure 3: Reconstructed  $\mu$ CT cross section through gerbil 1 (originally 1496x1496 pixels  
921 cropped to 740x950 pixels). a: middle ear air cavity, c: inner ear cochlea, i: incus, m: malleus,  
922 o: outer ear canal, s: stapes, t: tympanic membrane outline. Pixel size 8.5x8.5  $\mu$ m.

923

924

925

926

927

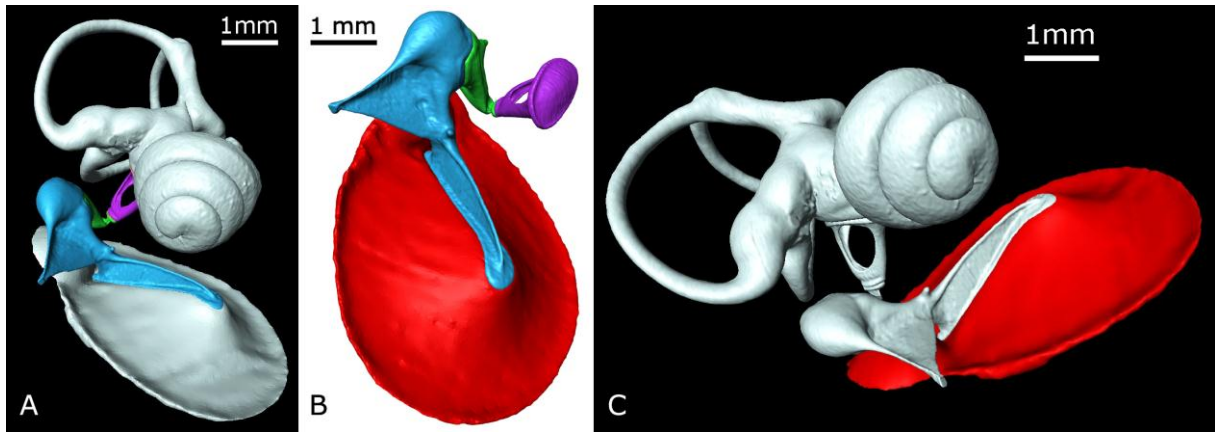
928

929

930

931

932



933

934 Figure 4: 3D surface meshes. Voxel size 8.5x8.5x8.5  $\mu\text{m}$ .

935 A) Tympanic membrane + middle ear ossicles + inner ear fluid (gerbil 1).

936 B) Tympanic membrane + middle ear ossicles (gerbil 2).

937 C) Tympanic membrane + middle ear ossicles + inner ear fluid (gerbil 3).

938

939

940

941

942

943

944

945

946

947

948

949

950

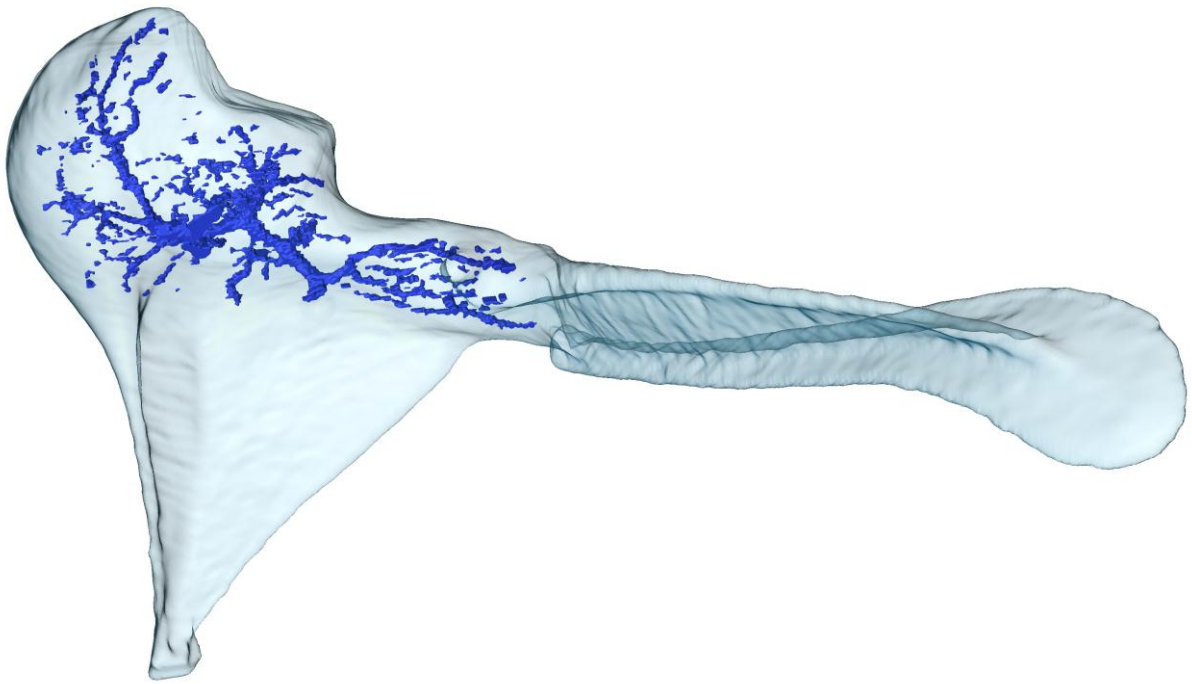
951

952

953

954

955



956

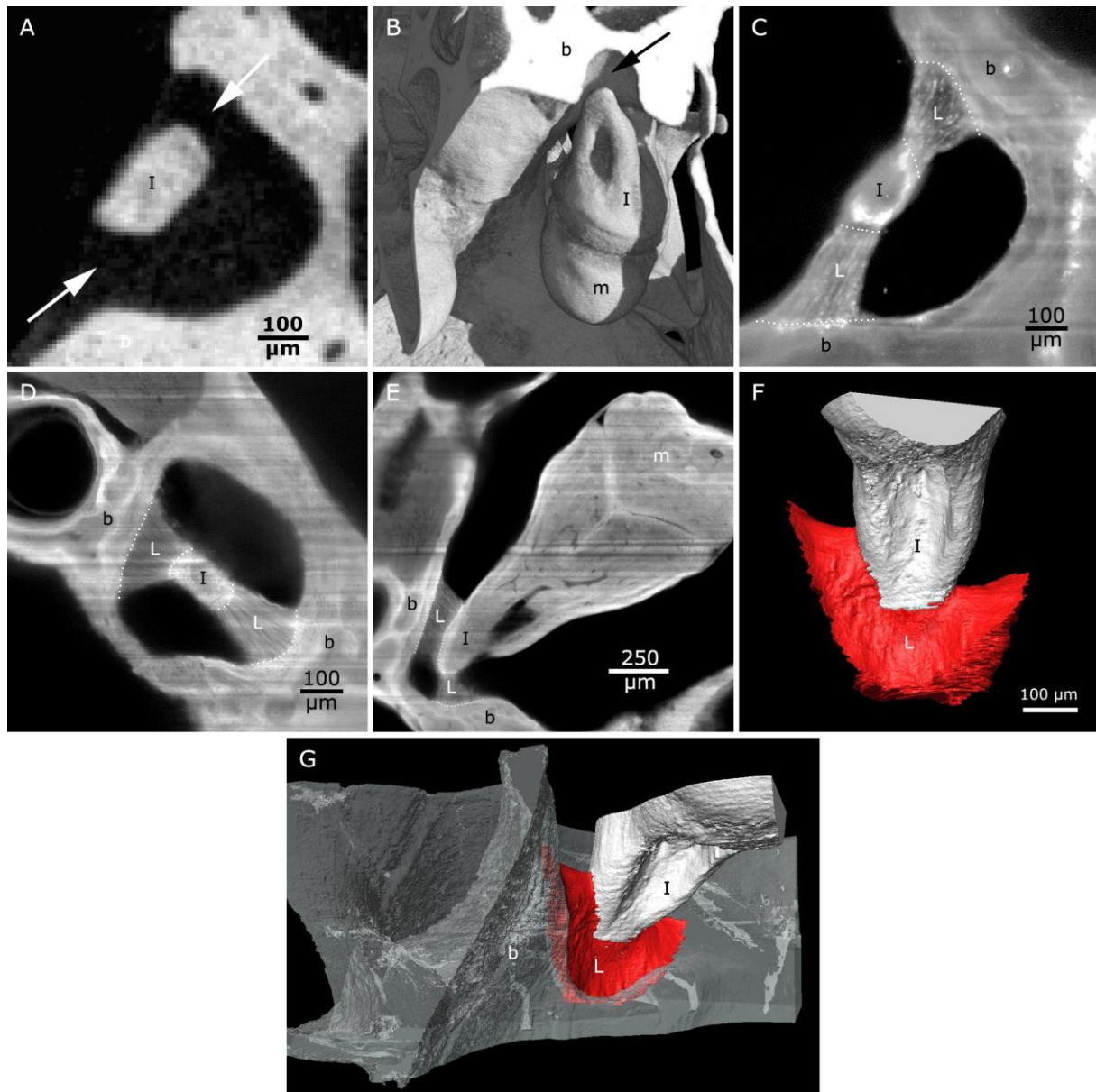
957 Figure 5: Mesh of the malleus (gerbil 2) rendered transparent in combination with a mesh of

958 the (major) blood vessel channels running inside it. Data obtained from  $\mu$ CT. Voxel size

959 8.5x8.5x8.5  $\mu$ m.

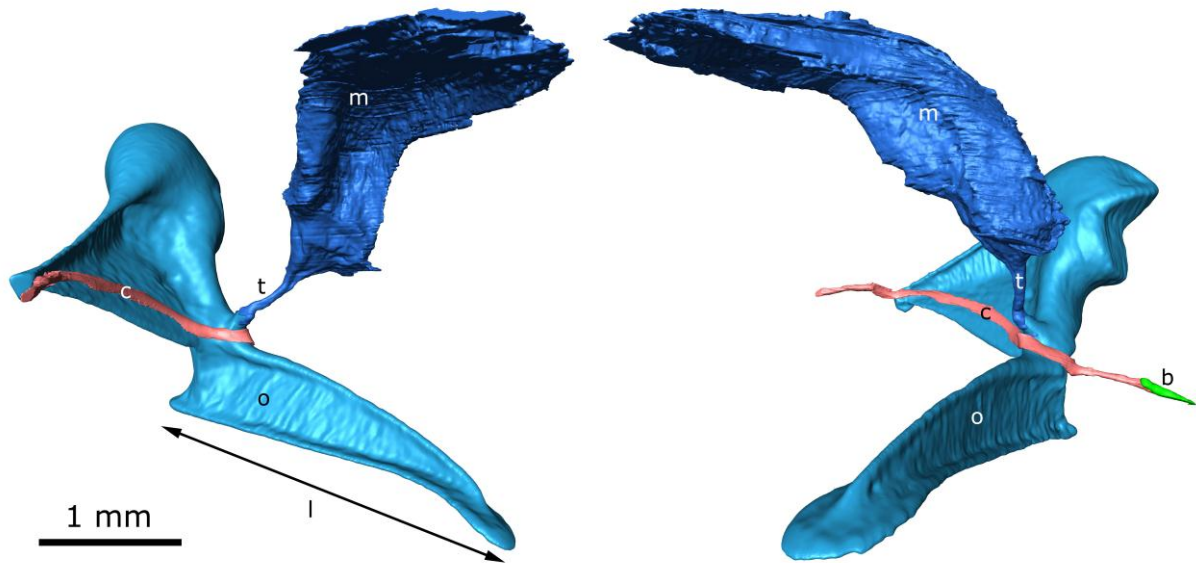
960





961  
 962  
 963  
 964  
 965  
 966  
 967

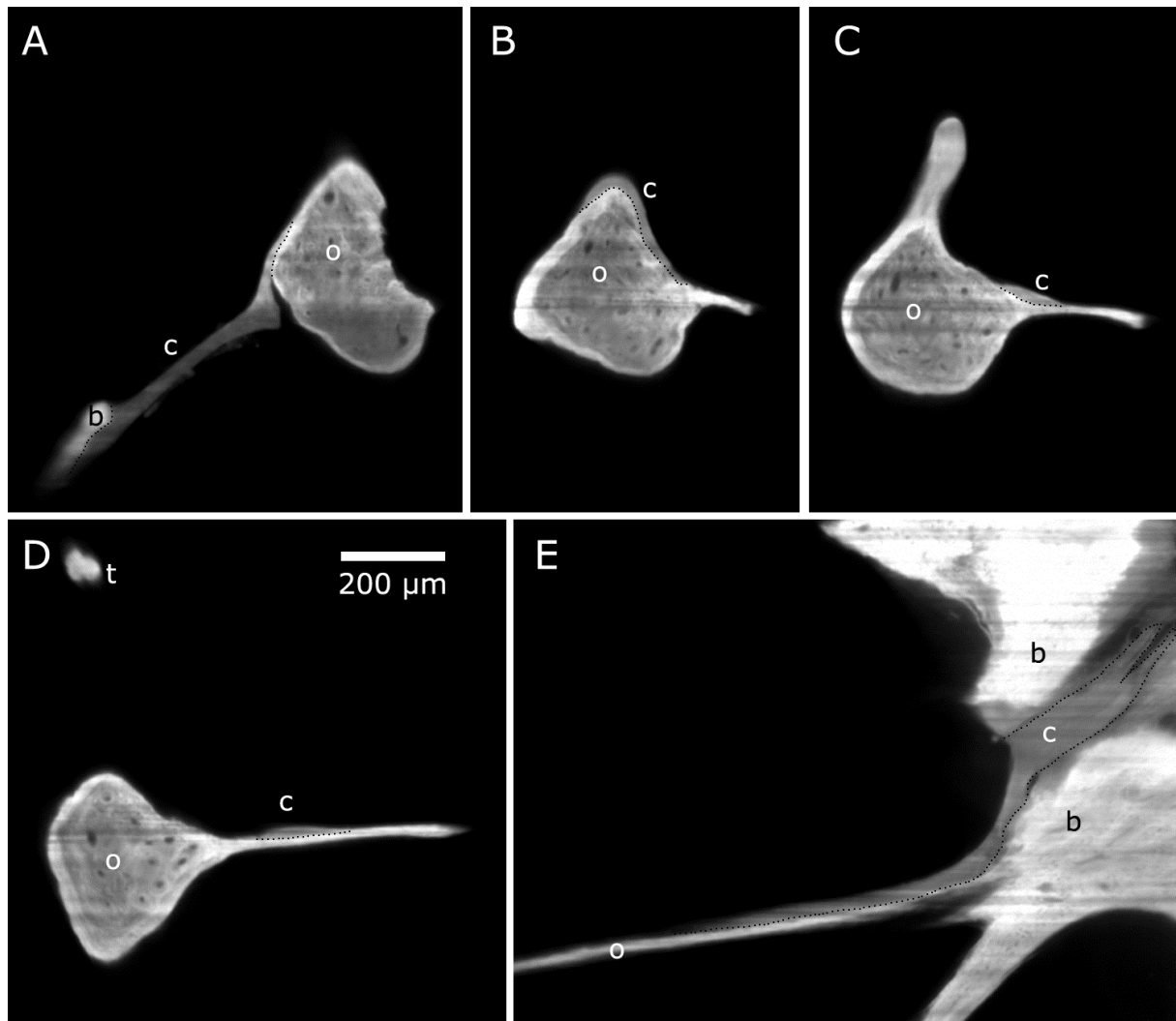
Figure 6: A)  $\mu$ CT cross section and B) 3D  $\mu$ CT reconstruction from automatic thresholding do not show the posterior incudal ligament in the bony wall recess. Arrows indicate the position of the invisible ligament. Pixel (and voxel) size  $8.5 \times 8.5 \times 8.5 \mu\text{m}$ . C-E) ROI OPFOS cross sections from different orientations do show the ligament in the recess. F-G) 3D OPFOS meshes. Voxel size  $0.97 \times 0.97 \times 2.5 \mu\text{m}$ . b: bulla, I: incus, L: ligament, m: malleus.



968

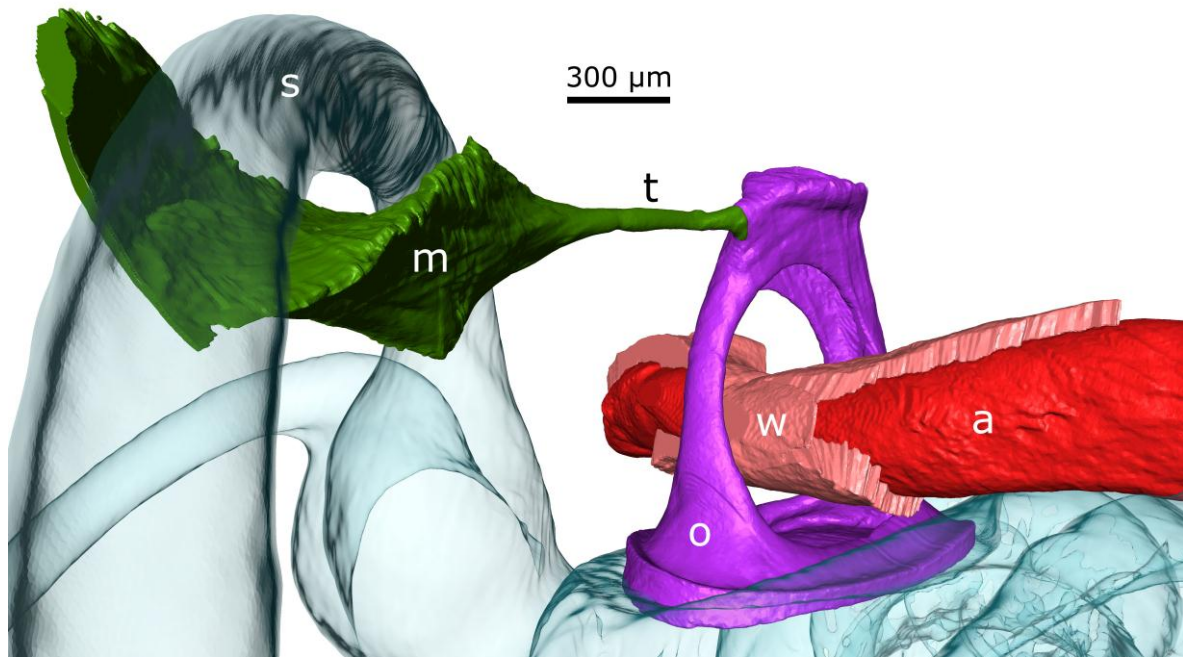
969 Figure 7: Two views of the topography of the chorda tympani in combination with the  
 970 malleus and the tensor tympani muscle & tendon (gerbil 2). The soft tissue data originate  
 971 from OPFOS (voxel size  $2 \times 2 \times 4.5 \mu\text{m}$ ), while the malleus data come from  $\mu\text{CT}$  (voxel size  
 972  $8.5 \times 8.5 \times 8.5 \mu\text{m}$ ). b: bulla, c: chorda tympani, m: muscle, o: malleus ossicle, t: tendon, l:  
 973 manubrium length.

974



975  
 976 Figure 8: OPFOS cross sections showing the course of the chorda tympani with respect to the  
 977 malleus. A) Chorda tympani jumps from a bony support beam to the malleus neck superior  
 978 side. B) It rounds the malleus neck below the tensor tympani. C,D,E) It continues on the  
 979 anterior process sheet until it enters a fissure in the bulla wall. b: bulla, c: chorda tympani, o:  
 980 malleus ossicle, t: tendon. All subfigures are of the same scale.

981  
 982  
 983  
 984  
 985



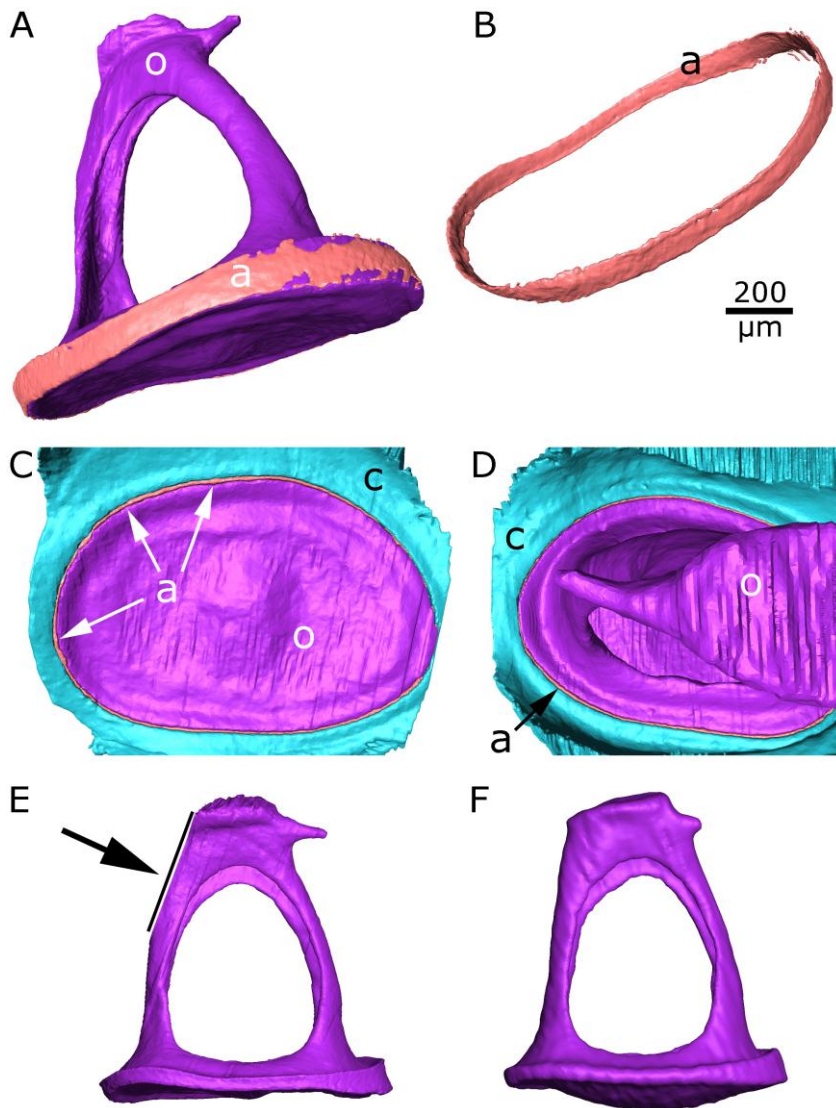
986

987 Figure 9: Stapes bone, stapedius muscle and tendon, and stapedial artery models obtained

988 from OPFOS (voxel size  $1.5 \times 1.5 \times 5 \mu\text{m}$ ), and the fluid-filled cavity of the horizontal semi-989 circular canal from  $\mu\text{CT}$  (voxel size  $8.5 \times 8.5 \times 8.5 \mu\text{m}$ ) are shown (gerbil 2). a: artery, m:

990 muscle, o: stapes ossicle, s: semi-circular canal, t: tendon, w: artery wall.

991



992

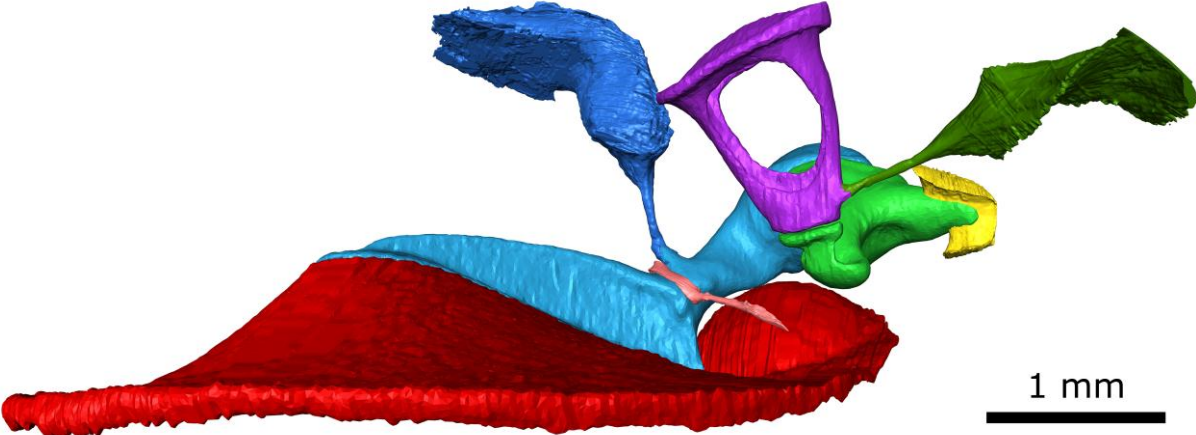
993 Figure 10: A-E) OPFOS based models of the stapes and the stapedial annular ligament (gerbil

994 2). F)  $\mu$ CT based model of the stapes (gerbil 2). The footplate modeled from  $\mu$ CT data is

995 convex, while in the OPFOS model it is not. a: annular ligament, c: cochlea, o: stapes ossicle.

996 The arrow indicates the end of the OPFOS dataset.

997



998

999 Figure 11: Merged OPFOS-CT ME model (gerbil 2).

1000

1001

1002

1003

1004

1005

1006

1007

1008

1009

1010

1011

1012

1013

1014

1015

1016

1017

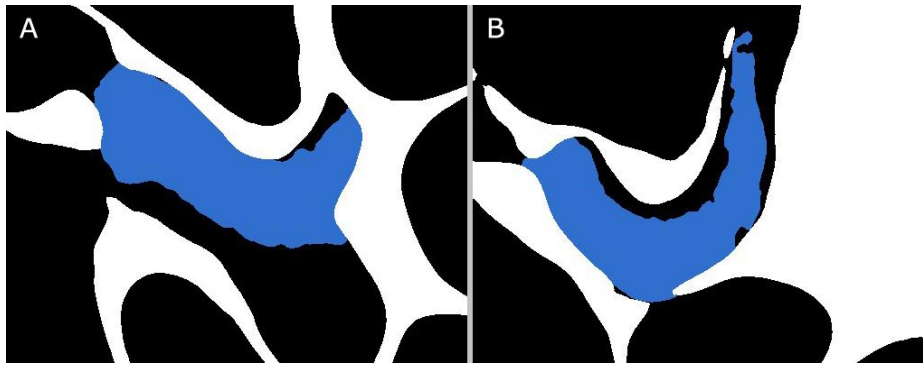
1018

1019

1020

1021

1022



1023

1024 Figure 12: Cross sections at different depths through the 3D merged models of the bulla  
1025 bone (white) from  $\mu$ CT and the tensor tympani (blue) from OPFOS. Black represents air filled  
1026 space such as the ME air cavity. The tensor tympani fits nicely in the bone, rather touching  
1027 the cavity wall than overlapping with it.

1028

1029

1030

1031

1032

1033

1034

1035

1036

1037

1038

1039

1040

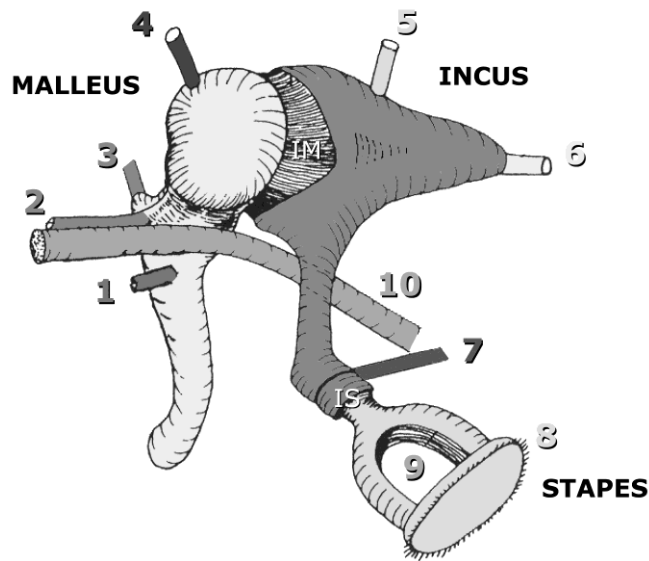
1041

1042

1043

1044

1045



**Ossicles:**

- M malleus BONE
- I incus BONE
- S stapes BONE

**Ossicle joints:**

- IM and IS cleft and LIGAMENT

**Ossicle suspension:**

- M.1 Tensor tympani TENDON
- M.2 Anterior mallear LIGAMENT
- M.3 Lateral mallear LIGAMENT
- M.4 Superior mallear LIGAMENT
- I.5 Superior incudal LIGAMENT
- I.6 Posterior incudal LIGAMENT
- S.7 Stapedial muscle TENDON
- S.8 Stapedial annular LIGAMENT

**Other soft tissue:**

- S.9 Stapedial ARTERY
- M.10 Chorda tympani NERVE

1046

1047 Figure 13: General schematic overview of all relevant middle ear components in human.

1048

1049

1050

1051

1052

1053

1054

1055

1056

1057

1058

1059

1060

1061

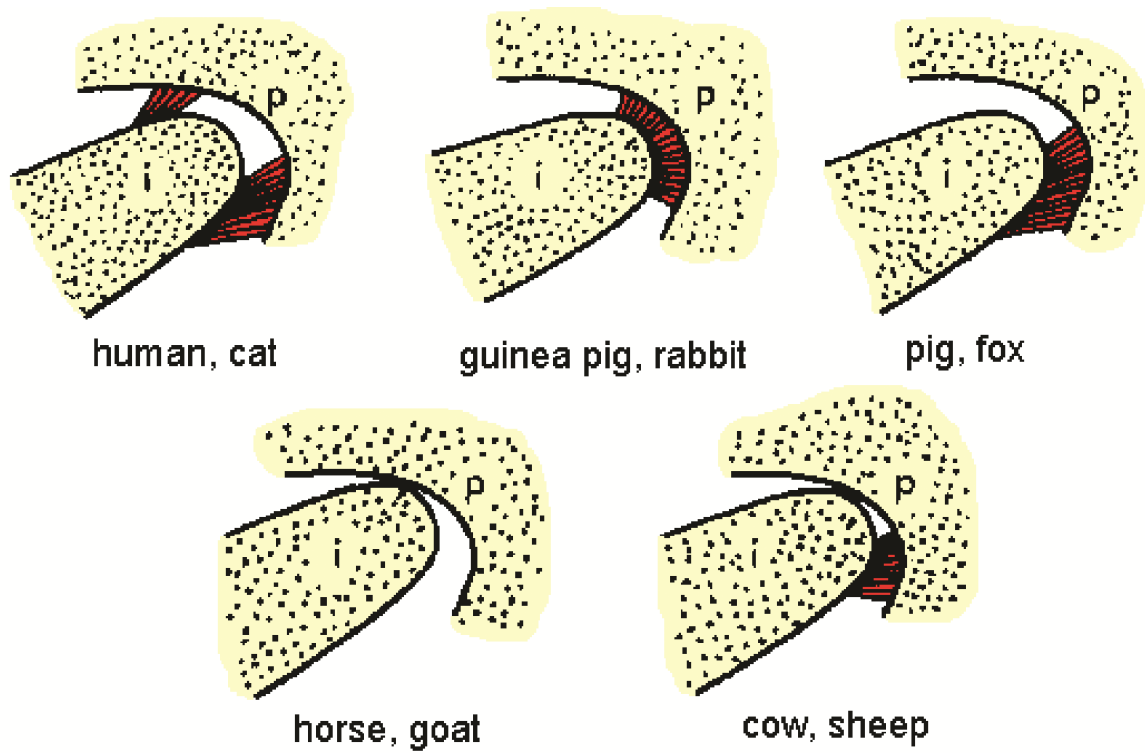
1062

1063

1064

1065





1066

1067

1068

1069

Figure 14: Schematic representation of different posterior incudal ligament configurations per species (courtesy of Funnell, 1972). Gerbil falls in the category of guinea pig and rabbit.